

Deep Learning based Prediction of MSI in Colorectal Cancer via Prediction of the Status of MMR Markers

Ruqayya Awan¹, Mohammed Nimir^{1,2}, Shan E Ahmed Raza¹, Johannes Lotz³, David Snead², Andrew Robison², and Nasir M. Rajpoot^{1,2,4}

¹Department of Computer Science, University of Warwick, UK

²Department of Pathology, University Hospitals Coventry & Warwickshire, UK

³Fraunhofer Institute for Digital Medicine MEVIS, Lübeck, Germany

⁴The Alan Turing Institute, London, UK

March 2, 2022

Abstract

An accurate diagnosis and profiling of tumour are critical to the best treatment choices for cancer patients. In addition to the cancer type and its aggressiveness, molecular heterogeneity also plays a vital role in treatment selection. MSI or MMR deficiency is one of the well-studied aberrations in terms of molecular changes. Colorectal cancer patients with MMR deficiency respond well to immunotherapy, hence assessment of the relevant molecular markers can assist clinicians in making optimal treatment selections for patients. Immunohistochemistry is one of the ways for identifying these molecular changes which requires additional sections of tumour tissue. Introduction of automated methods that can predict MSI or MMR status from a target image without the need for additional sections can substantially reduce the cost associated with it. In this work, we present our work on predicting MSI status in a two-stage process using a single target slide either stained with CK818 or H&E. First, we train a multi-headed convolutional neural network model where each head is responsible for predicting one of the MMR protein expressions. To this end, we perform registration of MMR slides to the target slide as a pre-processing step. In the second stage, statistical features computed from the MMR prediction maps are used for the final MSI prediction. Our results demonstrate that MSI classification can be improved on incorporating fine-grained MMR labels in comparison to the previous approaches in which coarse labels (MSI/MSS) are utilised.

1 Introduction

Our immune system acts as a natural guard against disease and infection-causing factors. It is very important particularly for cancer patients and is investigated for a number of reasons: its ability to defend the body against the cancer cells, cancer can affect the normal functionality of the immune system or in worst cases, immune system functionality deteriorates as a side effect of the cancer treatment. The principal component of the immune system is the white blood cells, also known as immune cells, made in our bone marrow. These immune cells have the ability to identify cancerous cells and kill them to prevent their growth. Tumour-infiltrating lymphocytes (TILs) are one of the kinds of immune cells that have been shown to exist in close proximity to cancer cells. Their presence indicates that the immune system is functional and responding against the tumour [1]. However, cancer cells can spread to the bone marrow and weaken the immune system by affecting the production of these blood cells. To boost our immune system fighting against cancer cells, there is a type of biological treatment known as Immunotherapy. It may help in the long-lasting revocation of cancer by training the immune cells to remember disease cells and fight if they ever come back. The studies have shown that the immune system may retain the benefits of immunotherapy even after the treatment has ended [2].

Immunotherapy has been proven to be a compelling treatment for some cancers when other traditional treatments such as chemotherapy become resistive. However, the number of patients who

would benefit from this treatment is limited. There are some predictive biomarkers for the selection of patients who are sensitive to this treatment. MMR status of the cancer is one of the most favourable biomarkers. MMR deficiency in the tumour is correlated with the efficacy of immunotherapy due to a high level of mutations [3]. This correlation has been extensively studied in colorectal cancers and similar findings are observed in other tumour types as well. In this paper, we present our work on identifying MMR expression for the end goal of predicting immunotherapy efficacy.

The MMR system is a highly sophisticated system for maintaining the integrity of DNA during replication and recombination and hence responsible for genomic stability [4]. It comprises MMR proteins which are dependent on four genes: mutL homologue 1 (MLH1), mutS homologue 2 (MSH2), mutS homologue 6 (MSH6) and postmeiotic segregation increased 2 (PMS2). These proteins repair the DNA by identifying errors occurring at microsatellites which are short repetitive DNA sequences. The differences in the length of the microsatellite between normal and tumour tissues of the same patient would indicate the deficiency in MMR and would lead to mutations of the above-mentioned genes. Tumours with variation in microsatellite length are known as MSI tumours and the ones with a high level of variations are termed as MSI high (MSI-H). There are two main methods for assessing the MMR status of the tumour: 1) IHC testing which is mainly used in clinical settings to detect MMR proteins and 2) PCR based methods for testing MSI. For PCR testing, National Cancer Institute (NCI) workshop in 1997 recommended following the Bethesda guidelines [5] on the five microsatellite markers known as the Bethesda markers. These markers consist of three dinucleotide loci (D17S250, D2S123 and D5S346) and two mononucleotide loci (Big Adenine Tract [BAT]-25 and BAT-26). Tumours showing instability at two or more markers are considered as MSI-H and when only one of the Bethesda markers is unstable then the tumour is interpreted as MSI-L. If none of the markers is unstable then the tumour is considered microsatellite stable (MSS). Both IHC and PCR testing methods have false-negative rates and are hence complementary to each other.

In our work, MMR expression status is determined by IHC for MMR proteins. The criterion for IHC testing is simple and straightforward which is the expression or complete loss of staining rather than scoring the intensity of staining as in ER/PR or HER2 IHC testing. In terms of loss expression, MLH1 and MSH2 form a pair with PMS2 and MSH6, respectively. Loss of MLH1 or MSH2 protein makes its partner unstable and hence would be accompanied by loss of expression of their respective partners. However, loss of expression of MSH6 or PMS2 will not affect their partners since they can bind to other molecules to maintain their stability [6]. In CRC, the DAB signal is observed in the nuclei of tumour cells only, for all the four MMR IHC assays. Nuclear staining in normal cells (lymphocytes, fibroblasts or epithelium) is considered as the internal positive control. A trained pathologist would assign a clinical status (Intact or Loss) to each case after evaluating the presence or loss of MMR staining. **Intact** status is assigned when an IHC assay shows the presence of DAB stain such that nuclear staining of tumour cells should at least have a similar or stronger intensity to that of internal positive control. The status of **Loss** protein expression is assigned when loss of DAB stain is detected in the tumour nuclei such that DAB staining intensity in cancerous nuclei is absent or less than that of the internal positive control. Identifying all four proteins as Intact indicates proficient MMR (pMMR) status while loss of expression in any one of the proteins indicates deficient MMR (dMMR) status.

In this study, our focus is on the detection of colorectal cancers cases with dMMR status which are likely to respond well to immunotherapy as compared to patients with pMMR status [7, 8]. We identify these cases using tissue slides stained with H&E and cytokeratin 8 (CK8) paired with cytokeratin 18 (CK18), referred to as CK818. In previous studies, CNNs are trained using MSI/MSS labels while in our work we have utilised MMR labels for training purposes in a two-stage process. On providing fine-grain MMR labelling, we show that our approach improves the performance of MSI/MSS classification in comparison to previous approaches.

2 Literature Review

MSI testing incurs additional cost and time and hence it is not performed for every patient in a clinical routine. Recently, researchers have been able to predict the MSI status directly from the H&E stained slides using deep learning and their encouraging results demonstrate that such an automatic system could enable MSI screening for every patient worldwide. Kather *et al.* [9] employed a trained CNN to classify tumour patches in a WSI into MSI or MSS class and finally, the class with a higher number of patches was used for assigning the WSI label. They later refined and tested this system on a large-scale

data [10, 11] and in [12], they perform MSI detection using the same approach without performing tumour segmentation as a preprocessing step.

Schmauch *et al.* [13] proposed a deep learning-based pipeline for predicting RNA-Seq profiles from H&E stained WSIs. The proposed pipeline comprises of two main steps. First, they perform CNN based feature extraction for randomly selected 8000 tissue tiles, resulting in a feature map of size 8000×2048 for each WSI. In the second step, they train a multi-layer perceptron referred to as HE2RNA for predicting gene expression for each tile. During the training stage, they take an average of different numbers (k) of the highest tile predictions at every iteration for deciding slide-level labels. At the inference stage, the slide-level label is obtained by taking an average of all tile-level labels obtained with every possible values of k . For MSI prediction, they simplified the above approach by averaging CNN features for every tile resulting in a feature map of size 1×2048 for every WSI and also modified the HE2RNA model accordingly.

Bilal *et al.* [14] proposed a novel deep learning framework for predicting status for a number of molecular pathways, including MSI. Their proposed framework comprises three models: first model (ResNet18) performs tumour segmentation, the second model referred to as iterative draw-and-rank sampling (IDaRS) selects the tiles with the most discriminatory features and the last model (HoVer-Net [15]) performs nuclei segmentation and classification into five different cell types. To predict slide-level labels, a linear support vector machine (SVM) was trained. Cell count for each category was used as a feature set for training an SVM. Their proposed method achieved an AUROC value of 0.90 which is significantly better than that of the state-of-the-art method [9] by 0.13.

3 MMR Panel Interpretation

The four MMR proteins (MLH1, PMS2, MSH2 and MSH6) exhibit nuclear staining patterns and are assessed for the presence and absence of brown staining produced due to the reaction of DAB substrate. MMR staining is likely to be observed in any normal cells such as lymphocytes, fibroblasts and normal epithelium. However, the MMR expression is only evaluated in nuclei of the tumour region while comparing their staining to that of normal cells acting as internal controls. Internal controls validated for the presence of staining are termed as internal positive controls. In the absence of staining in internal control, MMR protein expression cannot be evaluated and needs repeated IHC test either on the same or a different tissue block. A clear loss of nuclear staining in tumour cells in the presence of valid internal positive controls would indicate the Loss of protein expression, while a sample with unambiguous staining of tumour nuclei in the presence of valid internal positive controls would be identified as Intact protein expression. A loss of expression of DAB signal in any one of the MMR panels indicates that the patient may have germline mutation causing MMR deficiency, while the presence of DAB staining for all four MMR panels would designate the tumour as pMMR status. In Figure 1, visual fields extracted from WSIs of various staining patterns are shown.

Typically, MMR samples tend to show strong DAB signal. However, variability in the intensity of DAB staining can be observed from sample to sample. The staining variability in a tissue of the same sample is also not uncommon. For a sample to be given the Intact status, staining of the tumour nuclei should be at least equal or more than that of the internal positive control. As mentioned earlier, MMR proteins exhibit nuclear staining. However, there are chances of cytoplasmic staining. The possible causes of such unusual occurrences could be issues in IHC testing or a recently reported germline abnormality resulting in fusion of EPCAM and MSH2 [16]. In the presence of both cytoplasmic and nuclear staining, the IHC test is either repeated on the same block or a different block while only cytoplasmic staining pattern is considered as Loss of expression.

In a sample with Intact status, it is not uncommon to have a tissue area with the absence of protein staining. There are no standard criteria on an exact cutoff for normal protein expression. There are different propositions in literature for a cutoff of 1%, 5% or 10% [17] while The College of American Pathologists suggests that any amount of positive staining in the tumour nuclei is indicative of Intact status.

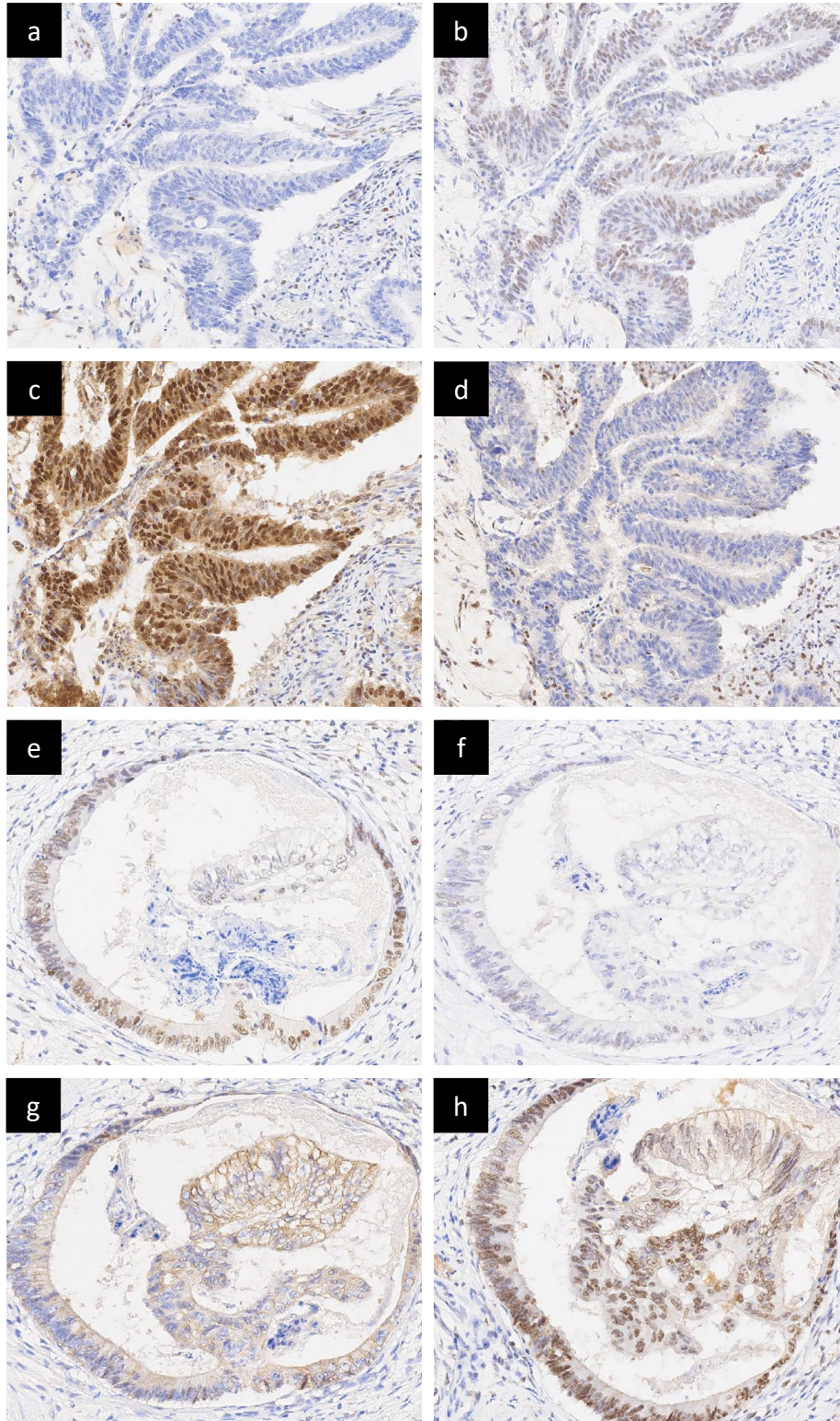


Figure 1: Visual fields taken from two cases with different MMR staining pattern. Case 1 (a-d): a) loss of MLH1, b) intact status of MSH2, c) intact status of MSH6 and d) loss of PMS2; Case 2 (e-h): a) intact status of MLH1, b) loss of MSH2, c) loss of MSH6 and d) intact status of PMS2. Notice the nuclear staining of internal positive controls (lymphocytes and stromal cells).

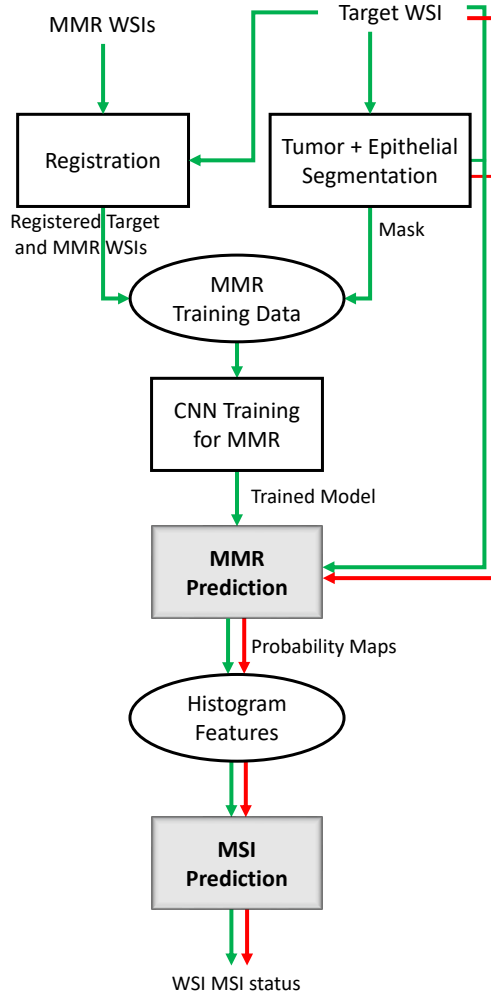


Figure 2: A block diagram showing the overall flow for the training and testing of our 2-step MSI classification procedure. Green lines corresponds to training stage while red line corresponds to inference stage.

4 The Proposed Method

A block diagram showing the overall flow for training and inference of the proposed method for prediction of the MSI status is shown in Figure 2. We performed a number of pre-processing steps: registration of MMR slides to the target image and tumour and epithelial segmentation. During registration, we spatially translate the H&E and MMR slides to align with the CK818 slide which is chosen as a reference image in this work. We perform tumour epithelial segmentation in order to restrict our MMR analysis to the epithelial area in cancerous tissue. This is because the pathologists analyse the nuclear staining of cancerous epithelial nuclei while deciding the status (Intact/Loss) of MMR slides. To this end, we perform tumour segmentation followed by epithelial segmentation. These two masks are then used to get epithelial regions in the tumour area.

4.1 Registration

A registration step in a co-localisation analysis workflow should be able to allow a significant spatial overlap between the two images such that the location of corresponding tissue structures can be determined. To this end, we employed a pipeline proposed in [18]. The pipeline comprises of three main steps: pre-processing, estimation of rigid alignment using ‘Deep Feature based Registration’ (DFBR) method, followed by a non-linear registration. During the pre-processing step, we generate

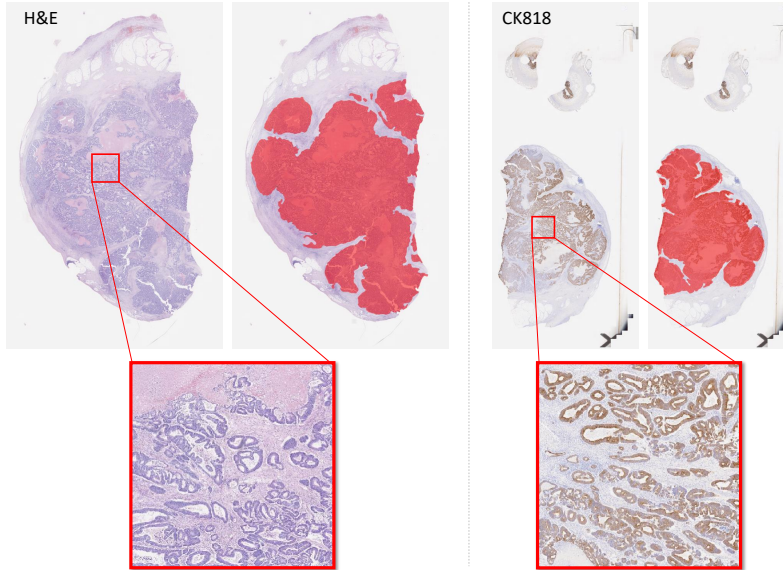


Figure 3: Tumour mask for H&E and CK818. Tumour masks overlaid on H&E and CK818 are shown in the left and right panels, respectively. Tumour mask was originally generated for H&E using a trained CNN model. Tumour mask for CK818 was generated by transforming the H&E mask using a transformation matrix computed using the DFBR method proposed in [18].

a tissue mask for an image pair and modify the input images such that they appear spatially similar. Our DFBR method further contains three sub-modules: *pre-alignment* to perform rough alignment, *tissue transform* estimates the transformation parameters using cropped tissue region and *block-wise transform* refines *tissue transform* by performing feature matching in a block-wise manner. After an image is registered using our DFBR, we observed a slight offset in some cases. To fix this offset, we added a local transform module which is followed by an existing non-linear registration method.

4.2 Tumour Segmentation

We trained a classification model using a publicly available colorectal adenocarcinoma dataset released with [19]. This dataset consists of 300 visual fields extracted at $20\times$ magnification of size around 7000×5000 pixels. These visual fields either belong to normal tissue or cancerous tissue. The cancerous visual fields were further classified into two categories: low-grade and high-grade cancer. Of 300 images, normal and low-grade classes comprise 120 images per class while the high-grade category comprises 60 images. We extracted patches of size 224×224 pixels for network training. We trained the Xception model using Adam optimiser with cross-entropy as an objective function. We generated a tumour mask for the CK818 image by applying geometrical transformation on the H&E mask. We used transformation parameters which were computed for registering the H&E image to CK818 image. A transformed H&E mask is shown in Figure 3.

4.3 Epithelial Segmentation

The MMR analysis should be restricted to the epithelial area in cancerous tissue, since presence or absence of positive staining in cancerous epithelial nuclei determines the status (Intact/Loss) of MMR markers. Taking this into consideration, one possible approach could be to perform epithelial nuclei segmentation. To this end, we used a publicly available dataset known as CoNSeP for training a cell segmentation network known as HoVerNet [15]. This dataset consists of 41 visual fields taken from 16 H&E stained colorectal adenocarcinoma WSIs. Each visual field is of size 1000×1000 , extracted at $40\times$ magnification. We performed stain deconvolution on input images to extract the H channel so that the same network could be used for the H&E and CK818 stained images. However, we didn't use nuclei segmentation masks for our analysis since the trained model didn't perform well. An example image from CK818 slide, its H channel and HoverNet predicted nuclei segmentation mask overlaid on

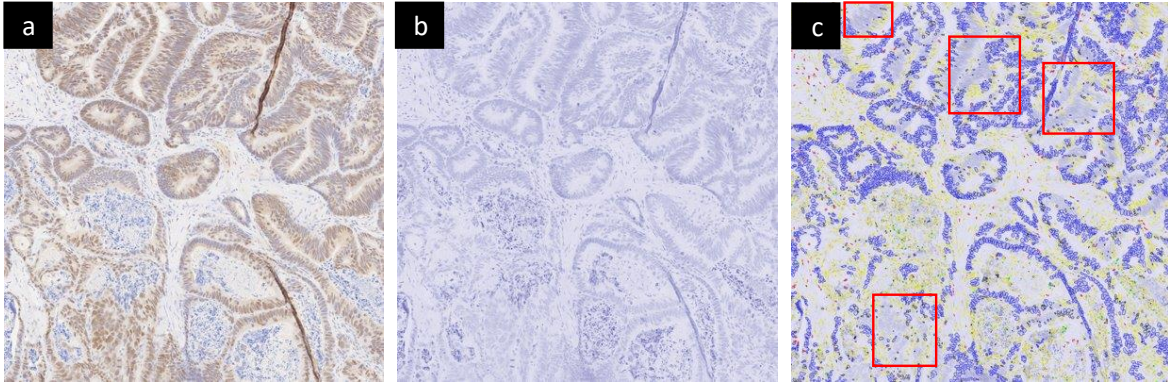


Figure 4: Visual results of nuclei segmentation using HoVerNet. a) CK818 image, b) H stain channel extracted from a), and c) nuclei segmentation mask overlaid on b). Blue colour is used for outlining the boundary of epithelial cells. Red blocks are used to highlight the area where epithelial nuclei are missed by the model.

H channel are shown in Figure 4. Another possible approach could be segmenting the epithelial layer which is less complicated in comparison to nuclei segmentation in terms of computational time and labelled data creation for training a model.

Unlike tumour segmentation, we didn't transform the H&E mask for generating the CK818 mask. Instead, we followed different approaches for CK818 and H&E images. This is due to the differences in tissue architecture (mostly visible at higher magnification levels) between H&E and CK818 images. We performed epithelial segmentation for H&E images using a UNET-like architecture. We used a publicly available dataset known as CRAG [20, 21]. This dataset consisted of 213 visual fields of size 1500×1500 pixels at $20 \times$ magnification, provided in two splits for training and validation. The train and valid sets comprise 173 and 40 visual fields, respectively. We manually annotated the epithelial layer in these images. To improve model performance on the COMET dataset, we also added 23 visual fields of size 2048×2048 from the COMET dataset for training purposes. We performed our experiments using input images at $20 \times$ and $10 \times$ magnification and didn't find a significant difference between their average DICE values. To accelerate the mask generation step, we finally used a model trained with images obtained at $10 \times$ magnification. We obtained a mean DICE value of 0.8645 on the CRAG validation set. The normal epithelial region was excluded by multiplying the predicted mask with the tumour mask.

Generating an epithelial mask for CK818 images was relatively straightforward. CK818 are known to have a cytoplasmic and membranous expression in glandular epithelial cells (both normal and cancerous). Considering this, an initial mask was created by a thresholding operation on the DAB channel and then we multiplied this mask with the tumour mask to get a final mask for tumour epithelial region. The predicted epithelial masks overlaid on the original CK818 and H&E stained images are shown in Figure 5.

4.4 MSI/MSS Classification

In previous studies, MSI classification is a one-step process where input is the H&E image and output is either MSI or MSS. Our proposed approach makes use of the MMR labels for predicting MSI status and hence we perform MSI prediction in two steps: MMR prediction followed by MSI prediction.

4.4.1 MMR Prediction

There could be at least two different strategies for learning MMR labels, either train separate CNN models for predicting each MMR label individually (as in [22] for ER/PR/HER2 prediction) or train a single multi-output CNN model. In this work, we opt the latter approach by implementing a multi-headed CNN architecture where each head is responsible for predicting a particular MMR staining expression status. The proposed CNN architecture is shown in Figure 8. We employed a partial Xception network as a backbone model while removing the last fully connected layer. The default

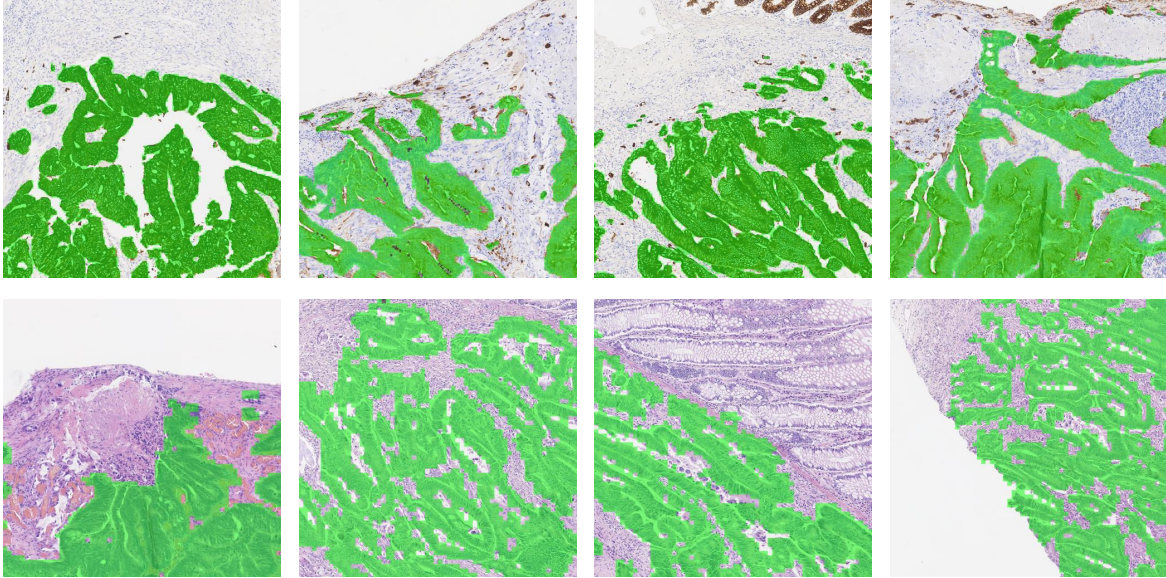


Figure 5: Epithelial mask generated by a trained CNN model. Top and bottom rows show overlaid images of CK818 and H&E images respectively. Images shown in third column contain normal epithelium which was excluded using the respective tumour mask.

input size for the Xception model is 299×299 . However, we selected a patch size of 512×512 pixels to include a bit more context. With an input size of 299×299 , the feature map generated by the last layer before pooling is of dimension $10 \times 10 \times 2048$ while with the 512×512 input, $16 \times 16 \times 2048$ feature map is generated. To reduce the spatial dimension of the resulting feature map, we added a convolutional layer before the global average pooling layer. After global pooling, the network is divided into four heads, each head comprises three fully connected layers. To prevent the model from overfitting, we added a dropout layer in the first two dense layers with a dropout rate of 0.5.

The ground truth data for the COMET dataset comprises MMR expression status (Intact/Loss) for a WSI. If we follow a weakly supervised strategy for training, then the WSI label could be assigned to each patch extracted from that particular WSI. However, as mentioned earlier, the MMR stained tissue slides with Intact status are likely to have some tumour regions without staining or variable staining. Keeping this into consideration, we adopt stain co-localisation for generating labels locally, rather than globally. We term this as a ‘localised’ setting for generating training data. Using this setting, we would get four binary labels against each input patch, where each label corresponds to an individual MMR protein. To this end, we first register the MMR slides to the target slide (CK818 or H&E). We then extract a patch from a target slide at $20 \times$ magnification using a tumour epithelial mask and the corresponding patches from the registered MMR slides. If the MMR expression label for a WSI is ‘Loss’ then we assign the ‘Loss’ label to every patch of that WSI. However, if the MMR expression label is Intact then we first compute the DAB stain intensity of a patch using the H-Score (as described below) and then perform thresholding to decide if the patch has Loss or Intact status. A pictorial demonstration of generating labelled data is provided in Figure 6. To compute the H-score, cellular staining intensity is first divided into four categories: strong (3+), moderate(2+), weak(1+) and no staining/negative(0). The summation of the weighted percentage of these intensity categories would compute the final H-Score value. We performed the following steps for computing the H-Score:

1. Deconvolve the IHC patch into H and DAB channels;
2. Threshold H channel to detect nuclei;
3. Using nuclei mask, we apply thresholding to each nuclei pixel in the DAB channel such that they fall into one of the four categories: strong (≥ 0 & ≤ 60), moderate (≥ 61 & ≤ 150), weak (≥ 151 & ≤ 200) and negative (≥ 201 & ≤ 255). Thresholding is performed after taking the complement of the DAB channel;

	MLH1	MSH2	MSH6	PMS2	Count
MSS	Intact	Intact	Intact	Intact	56
MSI	Loss	Loss	Loss	Loss	2
	Intact	Loss	Loss	Intact	1
	Loss	Intact	Intact	Loss	12
	Intact	Loss	Intact	Intact	1

Table 1: MMR ground truth labels for the COMET dataset.

4. Finally, we compute the H-Score using the following formula [23, 24]:

$$\begin{aligned} \text{H-Score} = & 3 \times (\% \text{ of nuclei stained at intensity category '3+'}) + \\ & 2 \times (\% \text{ of nuclei stained at intensity category '2+'}) + \\ & 1 \times (\% \text{ of nuclei stained at intensity category '1+'}) + \end{aligned}$$

5. The H-Score ranges between 0 and 300. On the basis of a discriminatory threshold, the patch status was considered either Intact or Loss. We selected a threshold value of 130.

We then train our multi-headed network using target input patches generated using our localised setting. We trained the model using Adam optimiser with binary cross-entropy as an objective function for each MMR label. We performed stain augmentation, rotation, flipping and elastic distortion for augmenting our training patches. Once the network is trained, we proceed to our second step for MSI prediction where we employ the trained model for generating MMR probability maps. We then extract features from these maps and utilise them for classifying each case as MSI or MSS.

4.4.2 MSI Prediction

Using the trained MMR model, we generate probability maps for all the train and test cases. For any given case, we get four probability maps, one per MMR biomarker. We then compute features for each MMR protein which is the histogram of probabilities of tumour epithelial patches. We use two histograms: one for protein Intact status and the other for protein Loss status. We selected the number of histogram bins parameter as 15 and normalised the histogram values. Finally, we input these features to an SVM classifier for WSI level MSI prediction. A diagrammatic illustration of MSI prediction step is shown in Figure 7. Note that MMR slides are only used during the training phase for labelled data generation. During inference we only use target slides for MMR and MSI prediction, hence ceasing the time burden of the pre-processing step of registration.

5 Dataset and Performance Measures

We used the COMET dataset obtained from the University Hospitals Coventry and Warwickshire (UHCW) NHS Trust in Coventry, UK. The dataset was provided after de-identification and informed consent was obtained from the patients. It comprises of 86 cancerous cases (of different patients) for our experiments on MSI prediction. There are 16 slides per case, each scanned using the Omnyx VL120 scanner at 0.275 microns/pixel. These slides are stained with different stains: CK818, Ki67, p53, Vimentin, MMR (MLH1, MSH2, MSH6 and PMS2), Ecadherin, EpCAM, PTEN and H&E and their exact sequence of staining is shown in 9. We considered six slides per case, involving MMR prediction from H&E and CK818 images for the end purpose of MSI prediction. For WSI-level MMR labels, we provided MMR tissue images along with their corresponding H&E to a pathologist. Of the 72 tumours out of 86, in which MMR analysis was possible, we obtained the expression status for each MMR slide. We then categorise these 72 cases into MSI and MSS using their MMR labels. Cases for which all the MMR slides were given Intact status were classified as MSS while any case with at least one MMR slide with Loss status was categorised as MSI. In total, we obtained 16 (22.2%) MSI and 56 (77.8%) MSS cases. The count of cases with different MMR and MSI ground truth labels are presented in Table 1. We assess the performance of our method by 5-fold cross-validation while keeping the same train and test set for CNN (MMR prediction) and SVM (MSI prediction) training and testing. We evaluated patch-level MMR prediction using DICE overlap and WSI-level MSI prediction using AUROC.

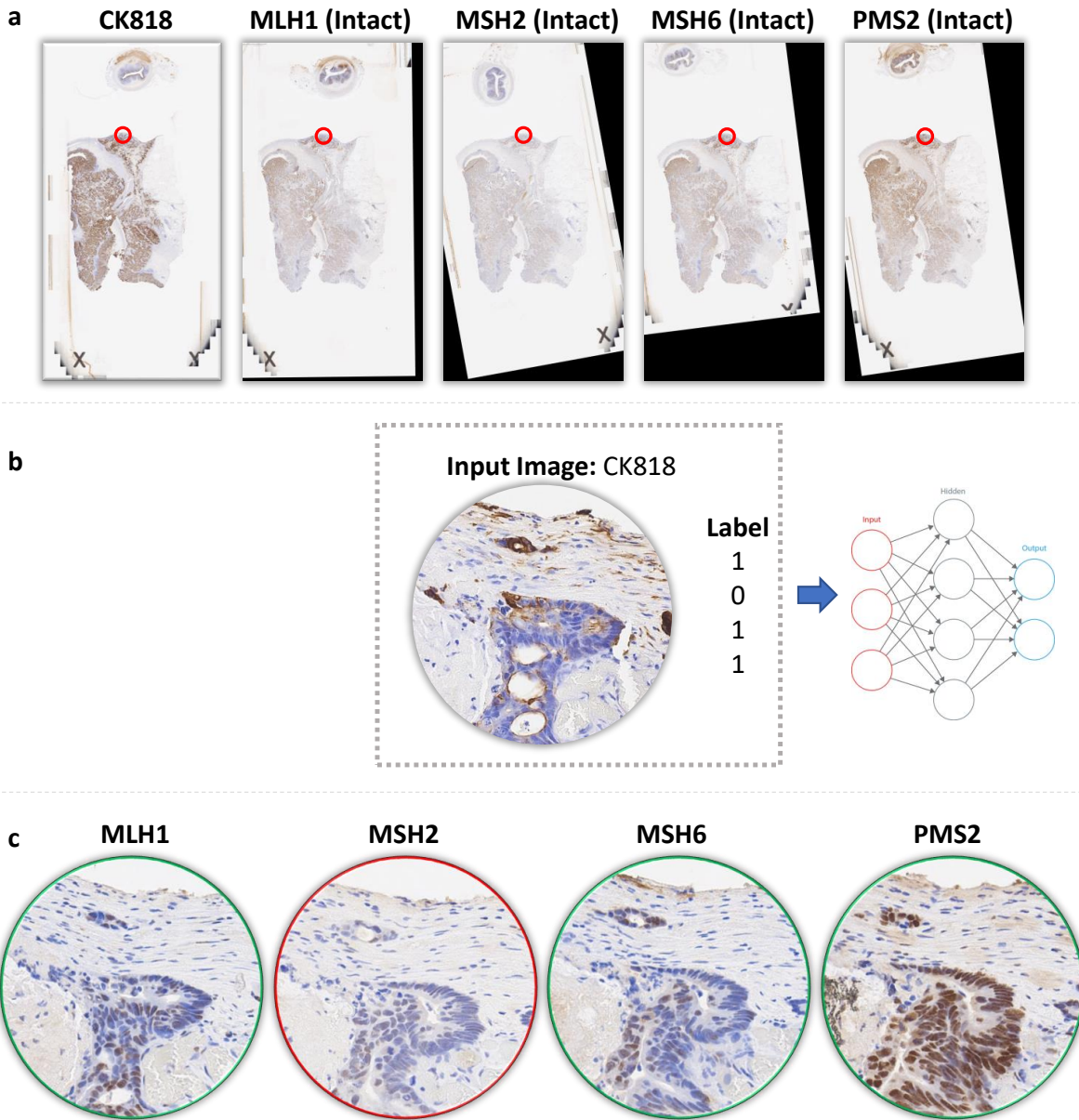


Figure 6: Co-localised MMR Prediction using CK818 as a target image. a) Downsampled WSIs of MMR IHC sections registered to CK818 stained WSI. b) An example input image used for training a CNN. Its ground truth label is defined by thresholding Hscore values computed for the corresponding patches from MMR slides. The corresponding MMR patches are shown in c). The colour of the borderline in c) shows the expression status for the given patch. Green represents that the patch is positively stained with DAB while red shows the absence of DAB stain. Patches shown in b) and c) are highlighted in red circles in a).

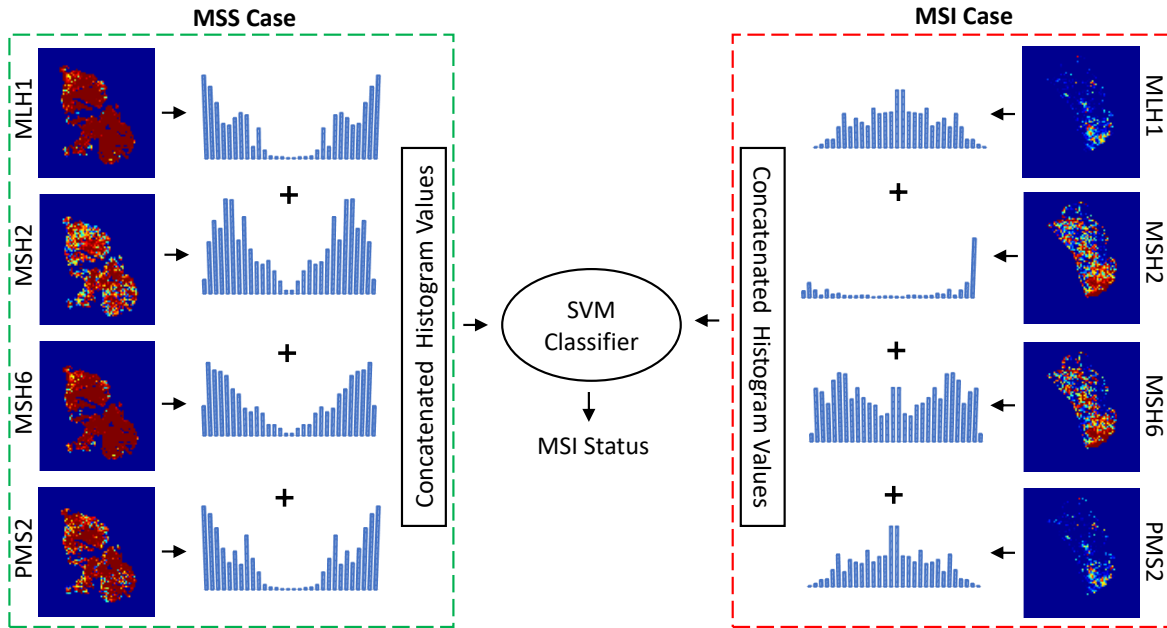


Figure 7: Overview of the proposed MSI prediction step. The MMR probability heatmaps and corresponding histogram of probabilities are shown for both MSS and MSI cases.

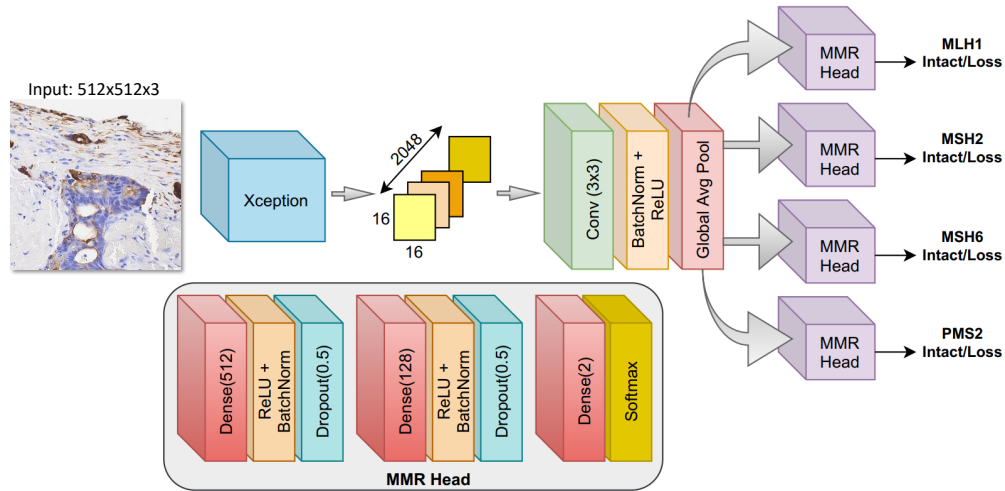


Figure 8: The proposed CNN architecture for MMR prediction.

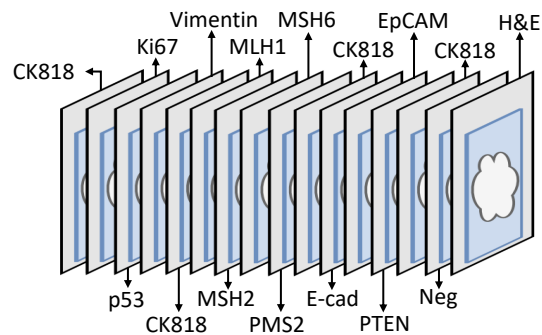


Figure 9: Sequence of multi-stained sections.

		Linear	Polynomial	RBF
CK818	Localised	0.9596±0.048	0.9444±0.062	0.9641±0.040
	Unlocalised	0.9051±0.124	0.9414±0.055	0.9429±0.067
H&E	Localised	0.8152±0.176	0.8455±0.149	0.9217±0.115
	Unlocalised	0.7798±0.179	0.7859±0.175	0.8313±0.180

Table 2: Average AUROC values for MSI prediction using 5-fold cross-validation obtained with different kernel functions in SVM.

6 Results and Discussion

We carried out two sets of experiments: one with a CK818 slide as a target image and the other with H&E slide as a target image. Below, we present our results of MMR and MSI classification steps for both CK818 and H&E slide images.

6.1 MMR Prediction

The MMR probability maps for Intact status overlaid on the original MMR tissue images are shown in Figure 10, along with the zoomed-in regions. We first computed the DICE overlap ratio to evaluate the performance of our multi-headed CNN model for MMR prediction. To this end, we generated the ground truth H-Score maps by processing MMR slides at 20× magnification in a sliding window fashion. The non-epithelial region was excluded while computing the H Score map. Thresholding was then performed to convert the H-Score maps to binary maps where foreground represents a region with Intact status while background represents a non-tissue region or a region with Loss status. The network-generated MMR probability maps were also converted to binary maps using a threshold value of 0.5.

We also performed a baseline experiment by directly utilising the MMR prediction maps for MSI classification, without training an SVM model. Thresholded probability maps were used for deciding Intact/Loss status for MMR proteins and it was based on the number of patches with Intact/Loss status. The Intact status was assigned if the number of Intact patches was more than the number of patches with Loss status. Finally, the MSI status was identified using these MMR labels. We obtained AUC of 0.8869 ± 0.150 and 0.8500 ± 0.124 for CK818 and H&E respectively, across 5-fold cross-validation data split. Figure 11 shows the results of MMR status prediction and its correlation with the pathologists’ MMR labels. On using MMR labels for CK818 as a target image, we were able to identify 98% and 75% of MSS and MSI cases, respectively. While for H&E as a target image, we correctly classified 95% of MSS and 56% of MSI cases, respectively.

6.2 MSI Prediction

We trained SVM models using histogram features with different kernel functions: linear, polynomial and RBF. We utilised our multi-headed network trained using two different settings for extracting histogram values. The localised setting is the one discussed in Section 4.4.1 while for unlocalised setting, slide-level MMR labels were assigned to all the patches rather than performing stain co-localisation analysis for generating labels. The average AUCs are reported in Table 2. The SVM with RBF kernel has been shown to outperform other kernel functions for both CK818 and H&E irrespective of any training setting. Our results suggest that the histogram values generated in the localised setting are more effective in classifying cases into MSI/MSS status as compared to those generated in an unlocalised setting. ROC curves for both CK818 and H&E based predictions for 5-fold cross-validation are shown in Figure 12.

6.3 Comparative Analysis

MSI cases can have different patterns of MMR expression, as observed in our dataset as well (see Table 1). Hence, in this regard, MMR labels can be considered as fine-grained labels of the coarse-grain MSS/MSI labelling. To the best of our knowledge, it is the first time that MMR labels are utilised for microsatellite (MS) classification. It is equally correct assigning MSI status to a case having an MMR pattern where at least one of the MMR proteins has a Loss status. Since our main task at

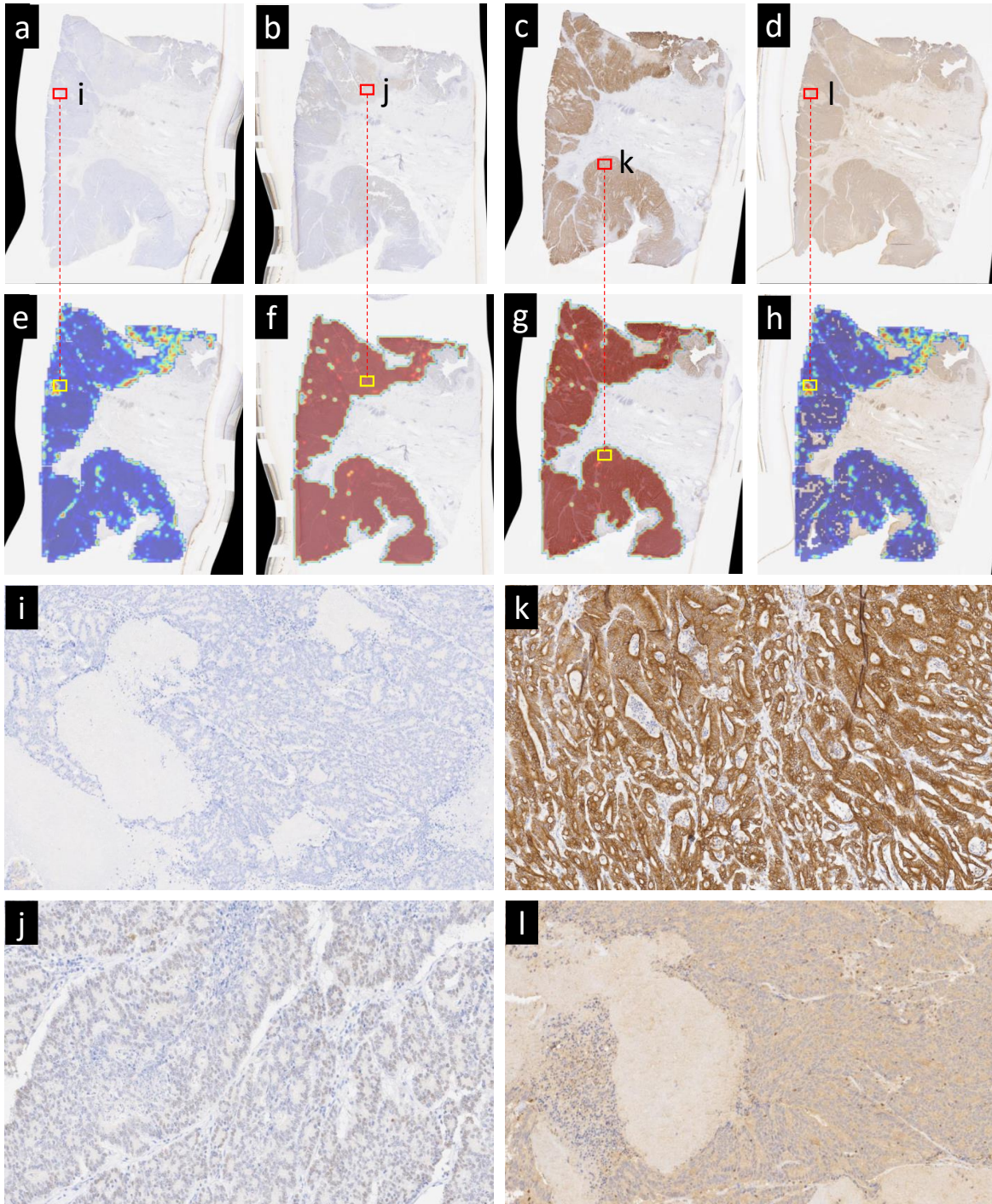


Figure 10: MMR prediction against CK818. a-d) MMR stained slides: MLH1, MSH2, MSH6 and PMS2, e-f) respective probability heatmaps overlaid on registered MMR stained WSIs, i-l) zoomed in patches highlighted on a-h with small rectangles. The ground truth MMR expression status for a-d is Loss, Intact, Intact and Loss.

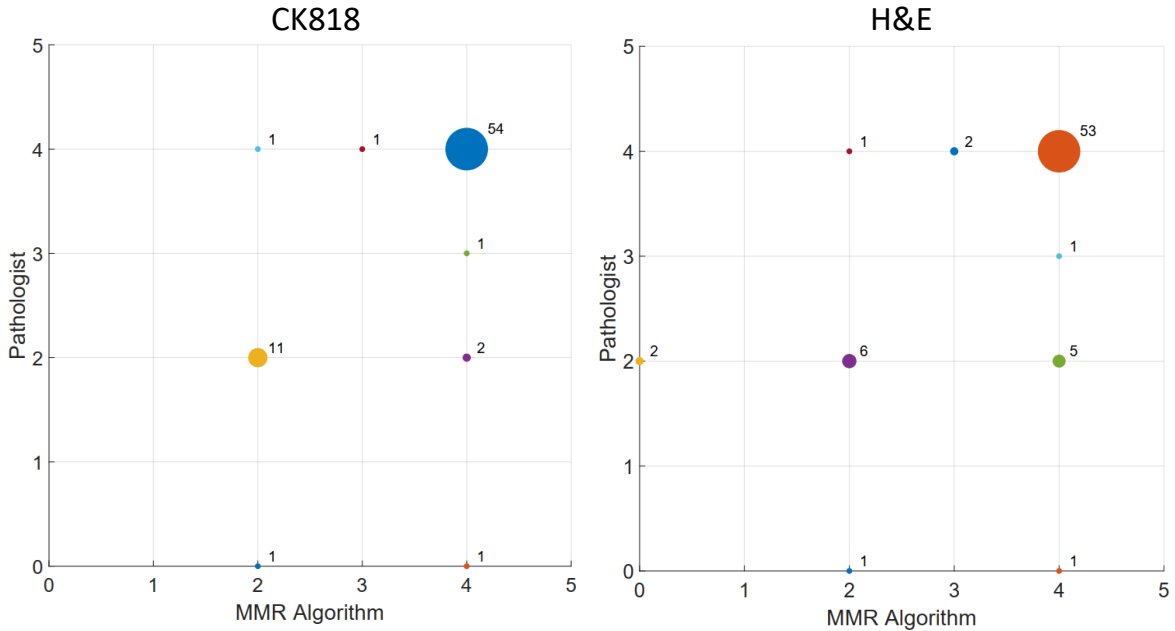


Figure 11: Scatter plot showing the WSI-level MMR prediction results using our baseline experiment in comparison to that of the pathologist’s assignment. Any MMR slide with Intact status is given a value of 1 while a slide with Loss status is given 0. This plot was generated by taking the sum of these MMR values. Size of the circular markers is relative to the number of cases with matching pathologist’s and algorithm generated labels.

hand in this study was to classify coarse-grained labels (MSS vs MSI), a question can arise: why not train a CNN using coarse-grain labels as it has been done in previous studies on MSI classification [9, 10, 11, 12, 13, 14]. In other words, is it beneficial to first train a CNN model with fine-grain labels (MMR labels) and then map them to coarse-grain labels (MSI/MSS) in a second phase?

Chen *et al.* [25] have shown that the CNN trained on natural images with fine-grained labels achieves better performance as compared to the network trained with coarse-grained labelled images of the same dataset. To study this with our dataset, we conducted another set of experiments, in which CNN was directly trained on MSI/MSS labelled patches instead of MMR labels. We trained the Xception network using Adam optimiser with binary cross-entropy as an objective function. The samples with a high proportion of MSI predicted patches to the total sum of MSI and MSS patches was labelled as MSI cases. We obtained AUC of 0.8646 ± 0.1152 and 0.8152 ± 0.1019 using the CK818 and H&E stained slides, respectively. In addition, similar to our approach discussed in 4.4.2, we trained an SVM using two normalised histograms of probabilities: one for MSS and the other for MSI and obtained AUC of 0.8465 ± 0.1391 and 0.8152 ± 0.1166 with CK818 and H&E stained slides, respectively. These results demonstrate that MSI classification can be improved on training CNN with fine-grain labels (MMR labels).

6.4 TCGA Cohort

To investigate the generalisability of our trained CNN model, we predicted MMR status in the patient cohorts from The Cancer Genome Atlas (TCGA). We experimented with colon and rectal cancer cohort (TCGA-CRC-DX) which was used in previous studies [9, 11, 14] on MSI prediction. The TCGA-CRC-DX cohort comprises a total of 428 WSIs, obtained from 423 patients. The ground truth labels of the cohort contain only MSI labels, not MMR expression status. To this end, we retrained our multi-headed network with all the H&E stained WSIs in the COMET dataset, followed by MMR prediction on the TCGA dataset. The training was performed in two separate settings: with stain augmentation and stain normalisation.

On visualising MMR prediction heatmaps overlaid on the H&E images, we mainly observed two patterns of MMR expression: pattern where most of the tumour regions are predicted as Intact (or

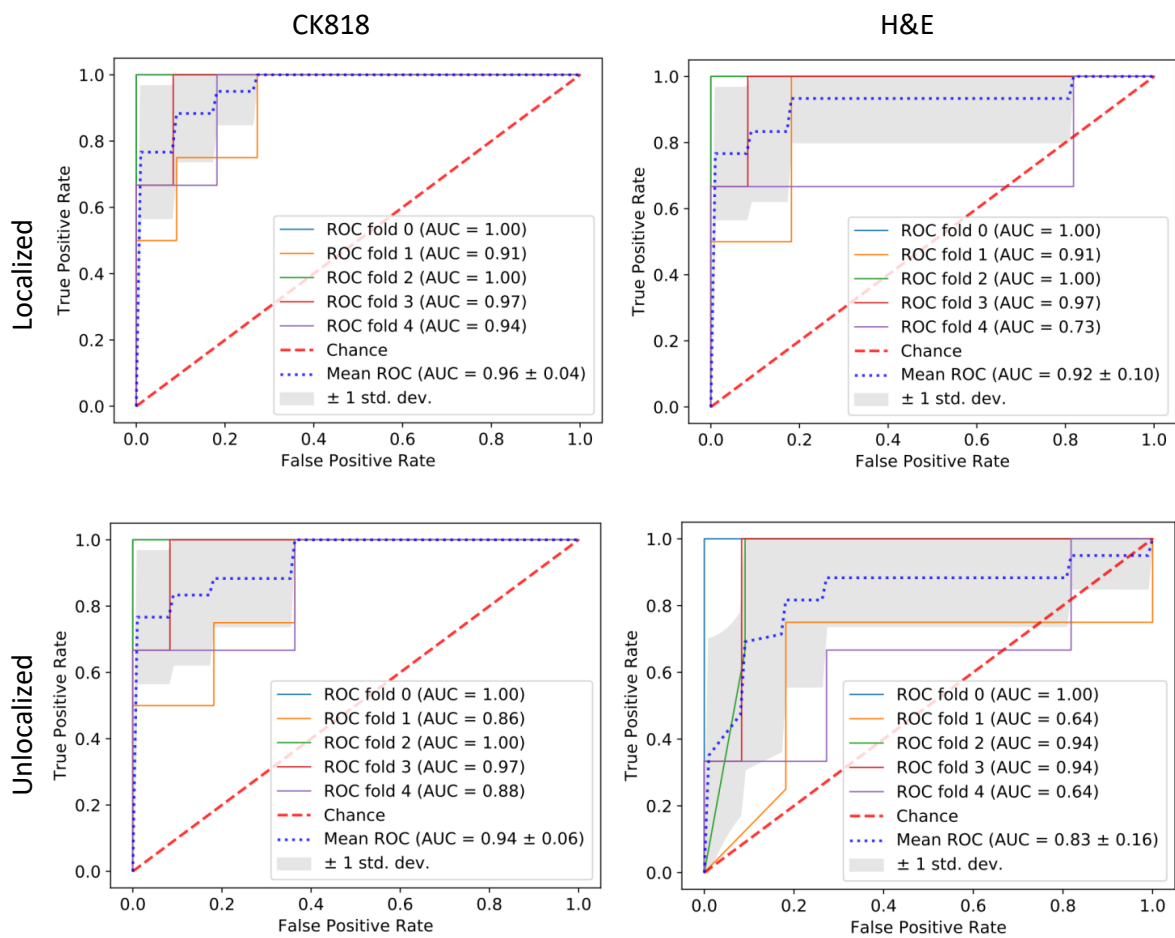


Figure 12: MSI Prediction on CK818 and H&E images using localised and unlocalised settings. AU-ROC plots of 5-fold cross-validation along with average AUROC is shown. For each curve, x- and y-axis represent false positive and true positive rates.

positive) for all the MMR markers (see Figures 14 and 15) and patterns where most of the tumour regions are predicted as Intact for MSH2 and MSH6 markers and Loss (or negative) for MLH1 and PMS2 markers (see Figures 13 and 16). We found that the trained model didn't generalise well for the TCGA dataset. Unlike our observation for the COMET cases, the aforementioned patterns were observed in both MSI and MSS cases, hence MMR heatmaps could not be used to extract discriminatory features for the TCGA dataset. Few example images in MSI and MSS subgroups with the overlaid predicted MMR heatmaps are shown in Figures 13 to 16. In Figures 13 and 15, we observed expected MMR expression for categorising this case as MSI and MSS, respectively, whereas in Figures 14 and 16, we observed unexpected MMR expression for categorising this case as MSI and MSS, respectively. We observed similar findings with both models, irrespective of their training strategies (stain augmentation or stain normalisation).

In computational pathology, model generalisation is a major challenge due to the domain shift. It is particularly prevalent when the model is trained on a small dataset, obtained from a single site with less diversity in terms of sample preparation and image acquisition. The problem of generalisation in our experiments is due to the same reason, the domain shift. Below, we list some possible elements contributing to the domain shift:

- Tissue samples for COMET were collected from a single site and all WSIs were acquired using Omnyx VL120 scanner while following the same acquisition protocols. The TCGA slides are collected from many sites across the USA. In addition to the multi-site aspect, the heterogeneity can also be characterised by the scanner modalities, manufacturers and acquisition protocols [26].
- The COMET and TCGA slides differ in terms of the stage of cancer. COMET slides were taken from the cancerous region described as either stage 3 or 4 while TCGA samples were taken from stage 1-4 cancers.
- We have looked at the distribution of histological type by MSI status in mucinous and non-mucinous cancer for both the COMET and TCGA cohort, as shown in Figure 17. The number of mucinous samples with both MSI and MSS status is significantly low for both datasets. Since our CNN model is trained on the COMET dataset, a total of 4 and 2 mucinous samples for MSI and MSS respectively are not adequate for learning discriminatory features for classification.

7 Conclusion

In this paper, we have presented a novel method for MSI classification in a two-stage process. The main focus is to perform MMR biomarker estimation from a single target image (CK818 or H&E) with an end goal of identifying cases with MSI status. To this end, we utilised registered images of the target and MMR tissue slides for identifying tissue regions with stain Intact/Loss status in a localised manner, rather than assigning a WSI label to every patch. Even with imperfections in MMR prediction maps, SVM was able to identify samples with MSI status. Our comparative analysis demonstrated improved performance of the CNN model if trained in a localised setting. Similar to the findings in previous literature, CNN trained with fine-grain MMR classes outperformed the CNN trained with coarse-grain MSI/MSS classes.

In clinical practice, identification of dMMR cases either using PCR or IHC testing incurs cost since it requires more tissue sections in addition to H&E stained section. Due to its high cost, not all patients are investigated that may lead to an inappropriate treatment plan for the patient. Patients with Lynch syndrome can potentially be imposed to chemotherapy rather than treated with immunotherapy, due to the lack of testing. Introduction of computational tools may assist the pathologists to overcome these issues and improve diagnostic performance and patient outcomes. The results of biomarker status prediction using computational methods such as those presented in our study are encouraging and can open routes for their applications in clinical workflows after further improvement and validation at a larger scale.

References

- [1] M. Peled, A. Onn, and R. S. Herbst, "Tumor-infiltrating lymphocytes—location for prognostic evaluation," *Clinical Cancer Research*, vol. 25, no. 5, pp. 1449–1451, 2019.

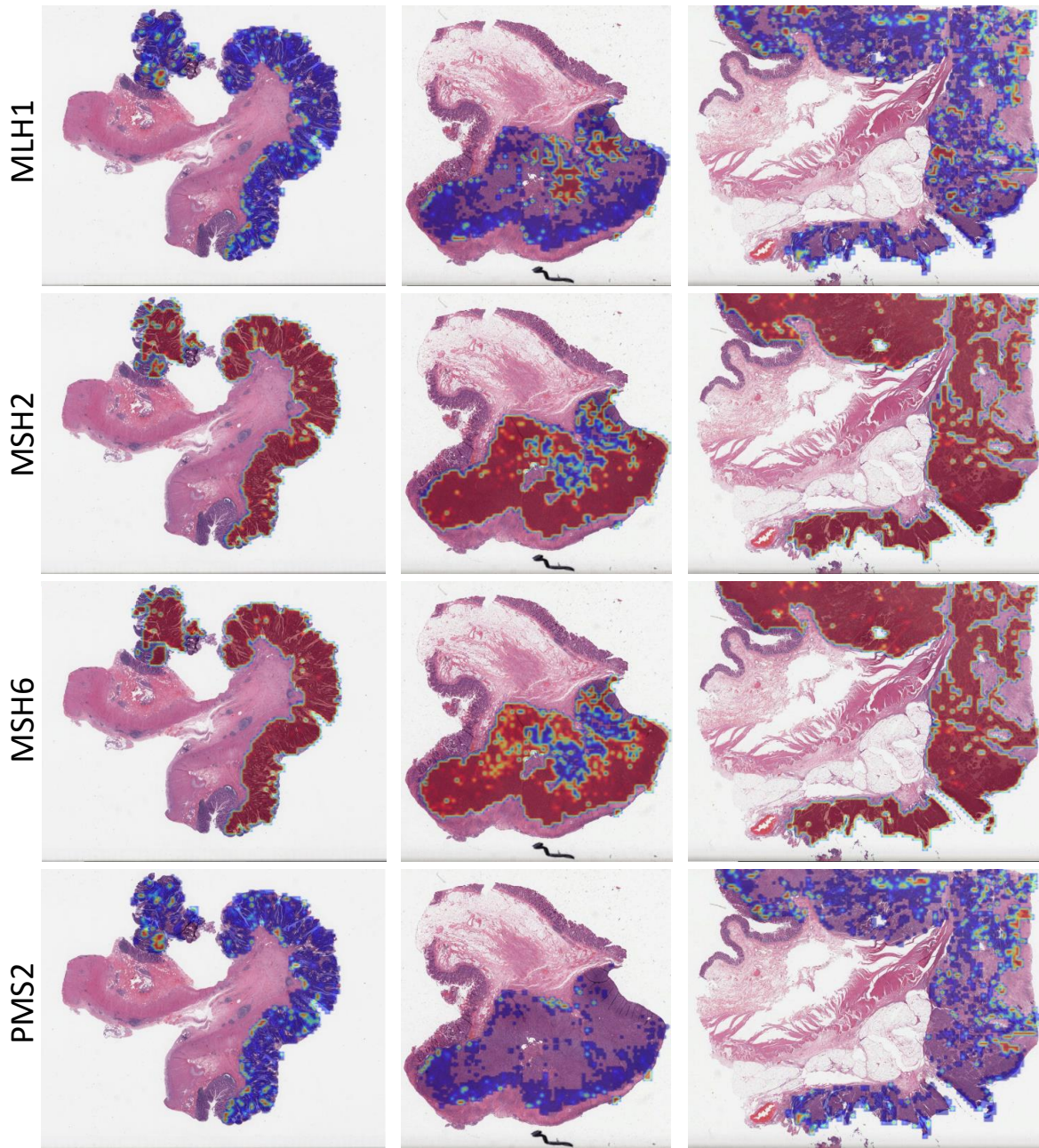


Figure 13: Example images from the TCGA cohort labelled as MSI. Our MMR model assigned probabilities of being positive (Intact) or negative (Loss) are used to generate a heatmap overlay for tumour region only. In the heatmap, red and blue colours correspond to the Intact and Loss class, respectively. The network has performed well for these images.

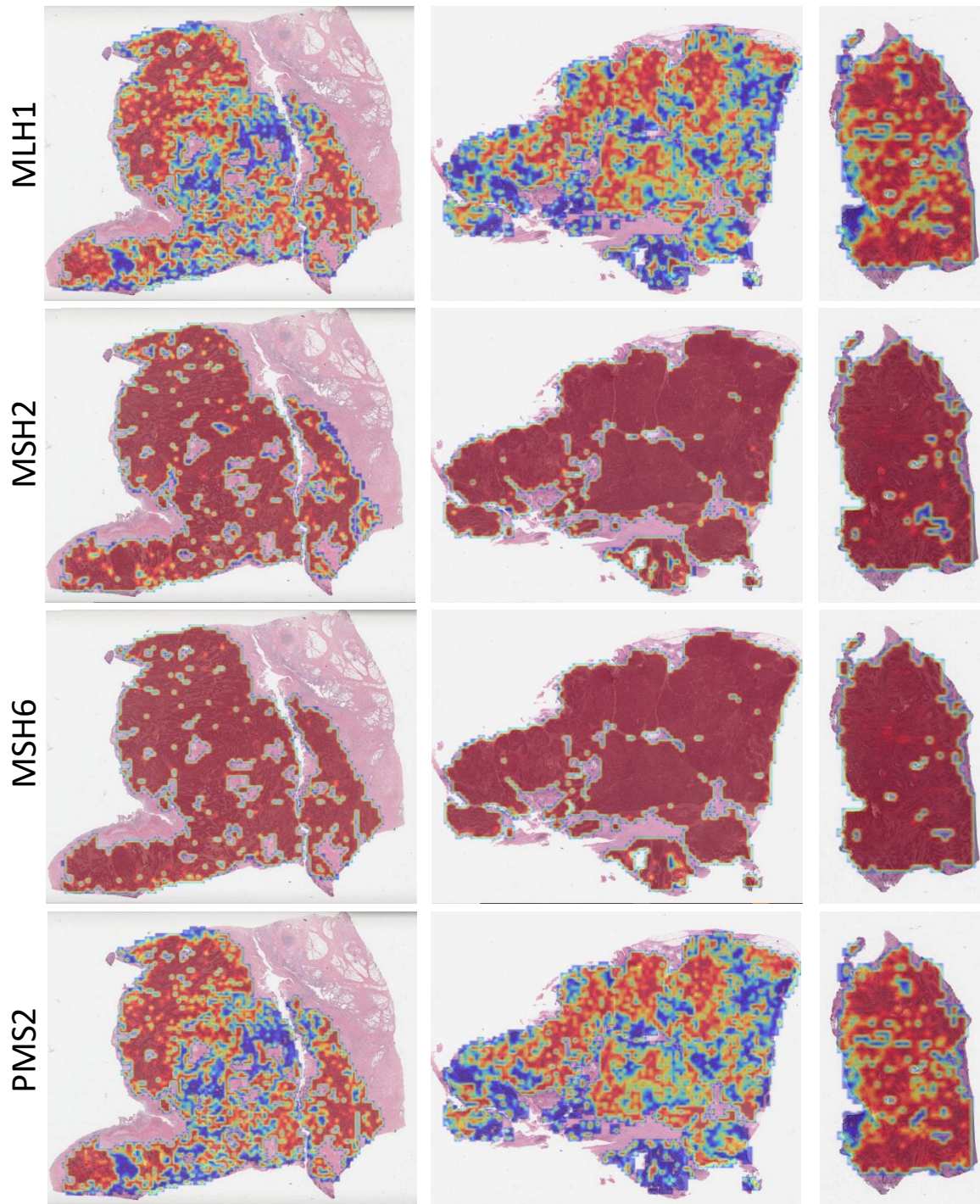


Figure 14: Example images from the TCGA cohort labelled as MSI. Our MMR model assigned probabilities of being positive (Intact) or negative (Loss) are used to generate a heatmap overlay for tumour region only. In the heatmap, red and blue colours correspond to the Intact and Loss class, respectively. The network has not performed well for these images.

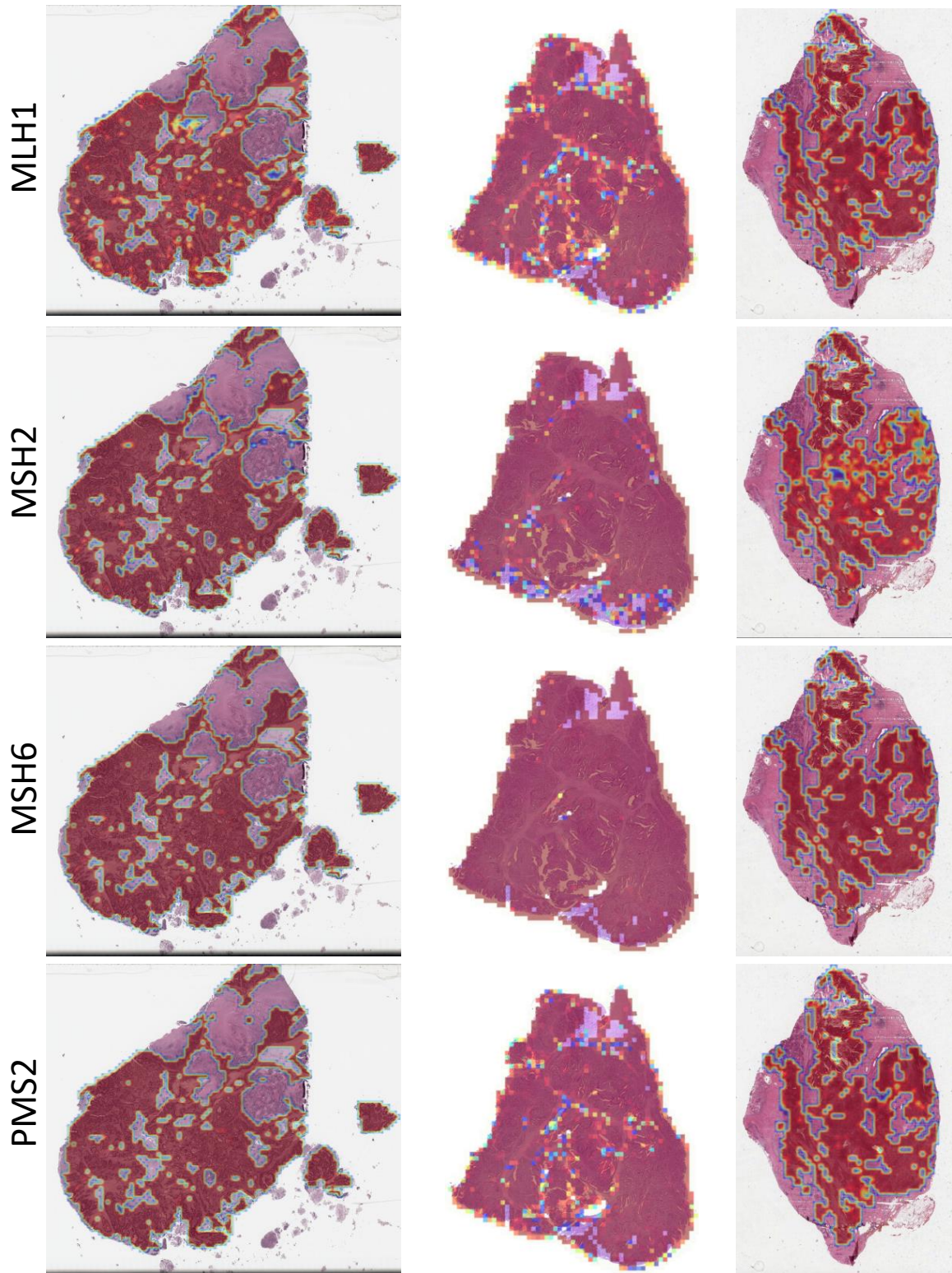


Figure 15: Example images from the TCGA cohort labelled as MSS. Our MMR model assigned probabilities of being positive (Intact) or negative (Loss) are used to generate a heatmap overlay for tumour region only. In the heatmap, red and blue colours correspond to the Intact and Loss class, respectively. The network has performed well for these images.

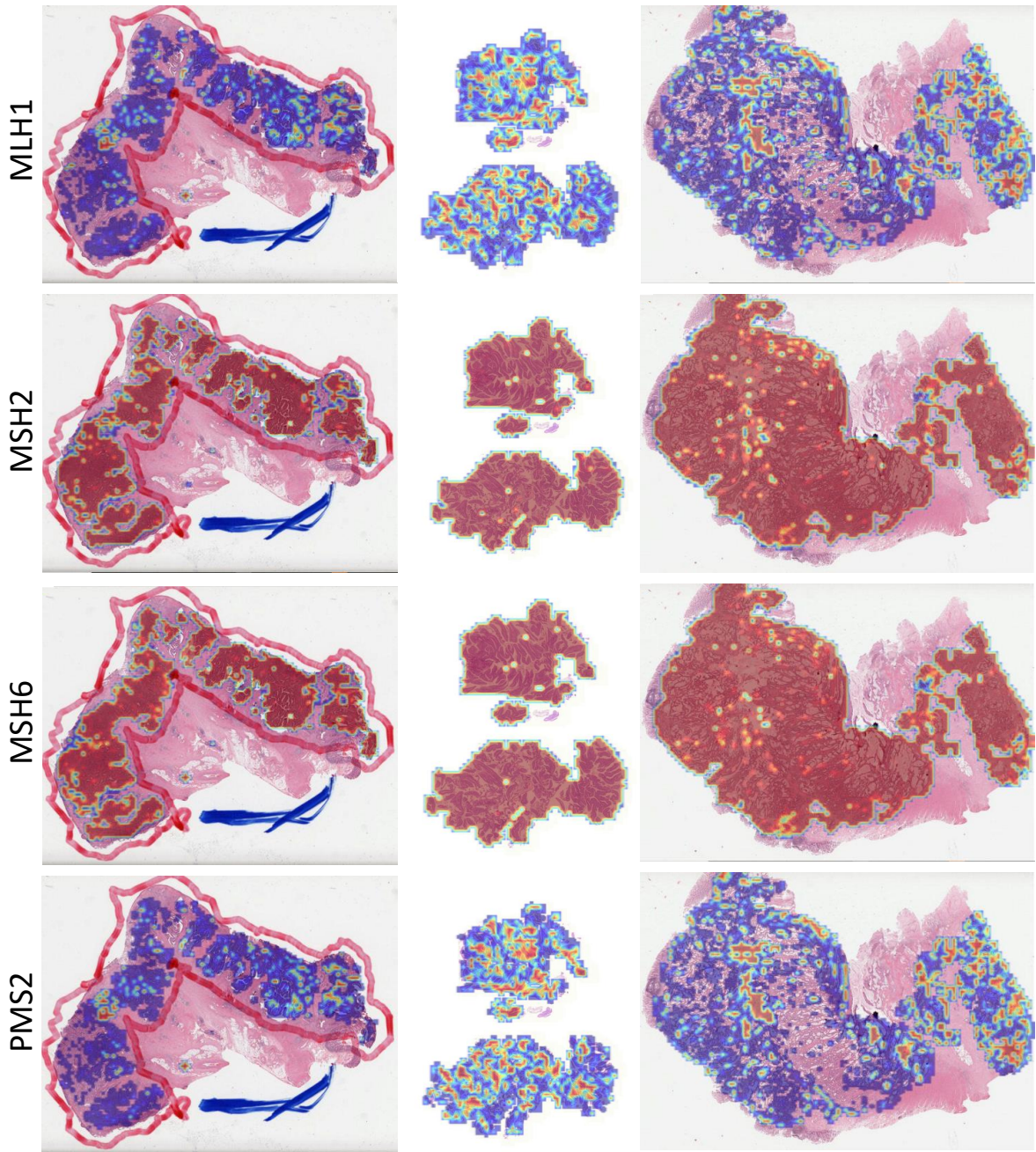


Figure 16: Example images from the TCGA cohort labelled as MSS. Our MMR model assigned probabilities of being positive (Intact) or negative (Loss) are used to generate a heatmap overlay for tumour region only. In the heatmap, red and blue colours correspond to the Intact and Loss class, respectively. The network has not performed well for these images.

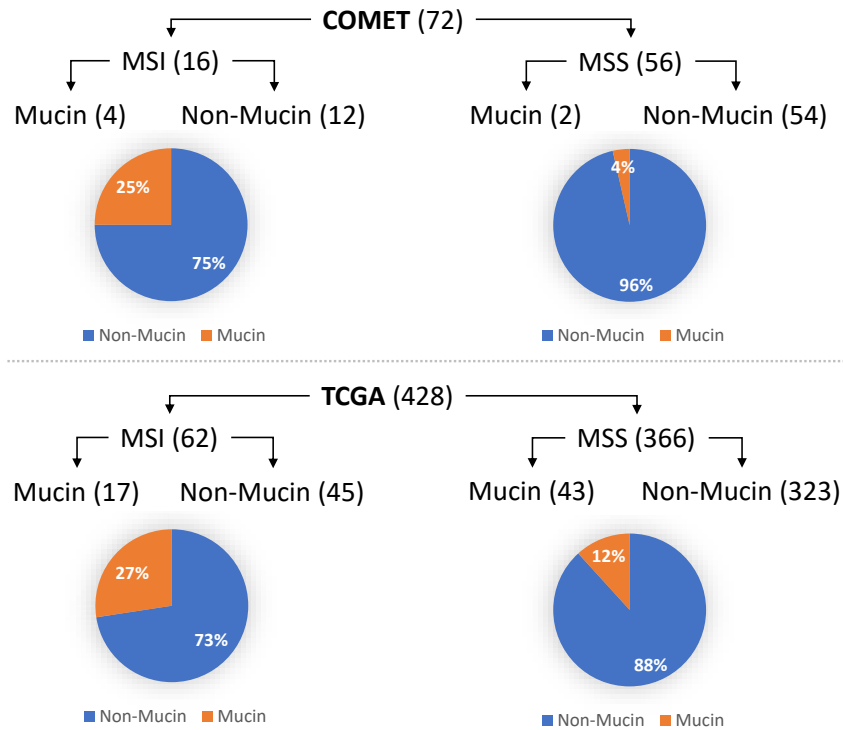


Figure 17: Comparison between TCGA and COMET cohorts in terms of the distribution of histological type (mucinous and non-mucinous) by MSI/MSS status.

- [2] K. Murata, T. Tsukahara, and T. Torigoe, "Cancer immunotherapy and immunological memory.," *Nihon Rinsho Men'eki Gakkai kaishi= Japanese journal of clinical immunology*, vol. 39, no. 1, pp. 18–22, 2016.
- [3] B. Timmermann, M. Kerick, C. Roehr, A. Fischer, M. Isau, S. T. Boerno, A. Wunderlich, C. Barmeyer, P. Seemann, J. Koenig, *et al.*, "Somatic mutation profiles of msi and mss colorectal cancer identified by whole exome next generation sequencing and bioinformatics analysis," *PLoS one*, vol. 5, no. 12, p. e15661, 2010.
- [4] P. Modrich, "Mechanisms in eukaryotic mismatch repair," *Journal of Biological Chemistry*, vol. 281, no. 41, pp. 30305–30309, 2006.
- [5] C. R. Boland, S. N. Thibodeau, S. R. Hamilton, D. Sidransky, J. R. Eshleman, R. W. Burt, S. J. Meltzer, M. A. Rodriguez-Bigas, R. Fodde, G. N. Ranzani, *et al.*, "A national cancer institute workshop on microsatellite instability for cancer detection and familial predisposition: development of international criteria for the determination of microsatellite instability in colorectal cancer," *Cancer research*, vol. 58, no. 22, pp. 5248–5257, 1998.
- [6] G.-M. Li, "Mechanisms and functions of dna mismatch repair," *Cell research*, vol. 18, no. 1, pp. 85–98, 2008.
- [7] M. P. Singh, S. Rai, A. Pandey, N. K. Singh, and S. Srivastava, "Molecular subtypes of colorectal cancer: An emerging therapeutic opportunity for personalized medicine," *Genes & Diseases*, vol. 8, no. 2, pp. 133–145, 2021.
- [8] E. C. Marginean and B. Melosky, "Is there a role for programmed death ligand-1 testing and immunotherapy in colorectal cancer with microsatellite instability? part ii—the challenge of programmed death ligand-1 testing and its role in microsatellite instability-high colorectal cancer," *Archives of pathology & laboratory medicine*, vol. 142, no. 1, pp. 26–34, 2018.

- [9] J. N. Kather, A. T. Pearson, N. Halama, D. Jäger, J. Krause, S. H. Loosen, A. Marx, P. Boor, F. Tacke, U. P. Neumann, *et al.*, “Deep learning can predict microsatellite instability directly from histology in gastrointestinal cancer,” *Nature medicine*, vol. 25, no. 7, pp. 1054–1056, 2019.
- [10] J. N. Kather, L. R. Heij, H. I. Grabsch, C. Loeffler, A. Echle, H. S. Muti, J. Krause, J. M. Niehues, K. A. Sommer, P. Bankhead, *et al.*, “Pan-cancer image-based detection of clinically actionable genetic alterations,” *Nature cancer*, vol. 1, no. 8, pp. 789–799, 2020.
- [11] A. Echle, H. I. Grabsch, P. Quirke, P. A. van den Brandt, N. P. West, G. G. Hutchins, L. R. Heij, X. Tan, S. D. Richman, J. Krause, *et al.*, “Clinical-grade detection of microsatellite instability in colorectal tumors by deep learning,” *Gastroenterology*, vol. 159, no. 4, pp. 1406–1416, 2020.
- [12] H. S. Muti, L. R. Heij, G. Keller, M. Kohlruss, R. Langer, B. Dislich, J.-H. Cheong, Y.-W. Kim, H. Kim, M.-C. Kook, *et al.*, “Development and validation of deep learning classifiers to detect epstein-barr virus and microsatellite instability status in gastric cancer: a retrospective multicentre cohort study,” *The Lancet Digital Health*, vol. 3, no. 10, pp. e654–e664, 2021.
- [13] B. Schmauch, A. Romagnoni, E. Pronier, C. Saillard, P. Maillé, J. Calderaro, A. Kamoun, M. Sefta, S. Toldo, M. Zaslavskiy, *et al.*, “A deep learning model to predict rna-seq expression of tumours from whole slide images,” *Nature communications*, vol. 11, no. 1, pp. 1–15, 2020.
- [14] M. Bilal, S. E. A. Raza, A. Azam, S. Graham, M. Ilyas, I. A. Cree, D. Snead, F. Minhas, and N. M. Rajpoot, “Novel deep learning algorithm predicts the status of molecular pathways and key mutations in colorectal cancer from routine histology images,” *medRxiv*, 2021.
- [15] S. Graham, Q. D. Vu, S. E. A. Raza, A. Azam, Y. W. Tsang, J. T. Kwak, and N. Rajpoot, “Hover-net: Simultaneous segmentation and classification of nuclei in multi-tissue histology images,” *Medical Image Analysis*, vol. 58, p. 101563, 2019.
- [16] S. Sekine, R. Ogawa, S. Saito, M. Ushiyama, D. Shida, T. Nakajima, H. Taniguchi, N. Hiraoka, T. Yoshida, and K. Sugano, “Cytoplasmic msh2 immunoreactivity in a patient with lynch syndrome with an epcam–msh2 fusion,” *Histopathology*, vol. 70, no. 4, pp. 664–669, 2017.
- [17] R. K. Pai and R. K. Pai, “A practical approach to the evaluation of gastrointestinal tract carcinomas for lynch syndrome,” *The American journal of surgical pathology*, vol. 40, no. 4, pp. e17–e34, 2016.
- [18] R. Awan, S. E. A. Raza, J. Lotz, and N. M. Rajpoot, “Deep feature based cross-slide registration,” 2022.
- [19] M. Shaban, R. Awan, M. M. Fraz, A. Azam, Y.-W. Tsang, D. Snead, and N. M. Rajpoot, “Context-aware convolutional neural network for grading of colorectal cancer histology images,” *IEEE transactions on medical imaging*, vol. 39, no. 7, pp. 2395–2405, 2020.
- [20] R. Awan, K. Sirinukunwattana, D. Epstein, S. Jefferyes, U. Qidwai, Z. Aftab, I. Mujeeb, D. Snead, and N. Rajpoot, “Glandular morphometrics for objective grading of colorectal adenocarcinoma histology images,” *Scientific reports*, vol. 7, no. 1, pp. 1–12, 2017.
- [21] S. Graham, H. Chen, J. Gamper, Q. Dou, P.-A. Heng, D. Snead, Y. W. Tsang, and N. Rajpoot, “Mild-net: Minimal information loss dilated network for gland instance segmentation in colon histology images,” *Medical image analysis*, vol. 52, pp. 199–211, 2019.
- [22] P. Gamble, R. Jaroensri, H. Wang, F. Tan, M. Moran, T. Brown, I. Flament-Auvigne, E. A. Rakha, M. Toss, D. J. Dabbs, *et al.*, “Determining breast cancer biomarker status and associated morphological features using deep learning,” *Communications Medicine*, vol. 1, no. 1, pp. 1–12, 2021.
- [23] S. Detre, G. S. Jotti, and M. Dowsett, “A” quickscore” method for immunohistochemical semi-quantitation: validation for oestrogen receptor in breast carcinomas.” *Journal of clinical pathology*, vol. 48, no. 9, pp. 876–878, 1995.

- [24] J. Liu, B. Xu, C. Zheng, Y. Gong, J. Garibaldi, D. Soria, A. Green, I. O. Ellis, W. Zou, and G. Qiu, “An end-to-end deep learning histochemical scoring system for breast cancer tma,” *IEEE transactions on medical imaging*, vol. 38, no. 2, pp. 617–628, 2018.
- [25] Z. Chen, R. Ding, T.-W. Chin, and D. Marculescu, “Understanding the impact of label granularity on cnn-based image classification,” in *2018 IEEE international conference on data mining workshops (ICDMW)*, pp. 895–904, IEEE, 2018.
- [26] “Tcga-coad.” <https://wiki.cancerimagingarchive.net/display/Public/TCGA-COAD>. Accessed 5 February 2022.